chemosensors

MDPI

Article

Origin of Baseline Drift in Metal Oxide Gas Sensors: Effects of Bulk Equilibration

Gerhard Müller [1,*] and Giorgio Sberveglieri [2]

[1] Department of Applied Sciences and Mechatronics, Munich University of Applied Sciences, D-80335 Munich, Germany
[2] Department of Information Engineering, University of Brescia, Via Branze 38, 25123 Brescia, Italy; giorgio.sberveglieri@unibs.it
* Correspondence: gerhard.mueller@hm.edu

Abstract: Metal oxide (MOX) gas sensors and gas sensor arrays are widely used to detect toxic, combustible, and corrosive gases and gas mixtures inside ambient air. Important but poorly researched effects counteracting reliable detection are the phenomena of sensor baseline drift and changes in gas response upon long-term operation of MOX gas sensors. In this paper, it is shown that baseline drift is not limited to materials with poor crystallinity, but that this phenomenon principally also occurs in materials with almost perfect crystalline order. Building on this result, a theoretical framework for the analysis of such phenomena is developed. This analysis indicates that sensor drift is caused by the slow annealing of quenched-in non-equilibrium oxygen-vacancy donors as MOX gas sensors are operated at moderate temperatures for prolonged periods of time. Most interestingly, our analysis predicts that sensor drift in n-type MOX materials can potentially be mitigated or even suppressed by doping with metal impurities with chemical valences higher than those of the core metal constituents of the host crystals.

Keywords: metal oxide gas sensor; electrical conductivity; sensor drift; oxygen vacancies; defect formation energy; Fermi energy

Citation: Müller, G.; Sberveglieri, G. Origin of Baseline Drift in Metal Oxide Gas Sensors: Effects of Bulk Equilibration. *Chemosensors* **2022**, *10*, 171. https://doi.org/10.3390/chemosensors10050171

Academic Editor: Marina N. Rumyantseva

Received: 27 March 2022
Accepted: 25 April 2022
Published: 2 May 2022

1. Introduction

Metal oxide (MOX) gas sensors sensitively respond to oxidizing and reducing gases in the ambient air. Although such sensors exhibit a broad-range response to a wide variety of different gases, their cross-sensitivity spectra can nevertheless be tuned to respond preferably to target gases of major interest in certain application scenarios and also to interfering gases which are likely to turn up in these scenarios [1]. With this capability of cross-sensitivity shaping at hand, arrays of sensors with different and well-chosen cross sensitivity profiles can be constructed to address different target applications. Examples of E-Nose gas sensors that address a number of target scenarios of recent interest are described in contributions presented at the latest GOSPEL conference [2–11]. A recent application of sensing biohazards in the International Space Station (ISS) is described in references [12,13].

An effect that can negatively impact the performance of E-Nose-type gas sensors is sensor drift. Sensor drift arises from slow changes in the sensor baseline resistance and in the gas response, thus mimicking apparent changes in target and interfering gas concentrations over time [14–17]. In case such changes impact different sensors inside an array with different intensity, sensor drift can also negatively affect the discrimination power of gas sensor arrays rather than simply mimicking gas concentration changes [18]. Taking an overall view over the available literature, it becomes apparent that the phenomena of sensor baseline drift and ensuing changes in gas response are receiving increasing attention, but that almost all of those approaches aim at mitigating and correcting drift effects by algorithmic means [19–29].

In this paper, a different approach to the problem of sensor drift is presented which is more hardware-related and which aims at identifying and controlling those physical processes that drive the processes of sensor drift and sensor degradation. In the following, it is shown that MOX gas sensors feature an intrinsic tendency of drifting to increasingly higher baseline resistances R and of lessening gas-induced resistance changes ΔR in the course of time, however, with the ratios $\Delta R/R$ remaining approximately constant over time. It is argued that these changes originate from the fact that n-type metal oxides are not normally doped with foreign impurities with chemical valences different than those of the core metal ions inside the MOX lattices, but rather by thermally generated oxygen vacancies. Such vacancies are normally generated during high-temperature materials preparation and become quenched in during cool-down after preparation. Representing non-equilibrium entities, such thermal donors tend to slowly relax towards lower densities, causing MOX materials to slowly drift towards lower baseline conductivities and lessening capabilities of accumulating negative oxygen ion adsorbates at their surfaces, which limits their reducing gas response. Perhaps, the most interesting conclusion is that sensor drift effects might be mitigated or even suppressed by doping the MOX materials with metal impurities with higher chemical valences than the constituent metals of the core crystals.

2. Experimental Evidence for Sensor Drift

The effects of long-term sensor drift in MOX materials were investigated by the Brescia group in the course of the S3 project [15]. There, the drift effects in SnO_2 nanowire materials were investigated which had been deposited at very high temperatures using the solid–liquid–vapor (SLV) condensation technique [30,31]. The nanowires were deposited on ceramic substrates with pre-deposited platinum (Pt) interdigital electrodes on the front side and Pt heater meanders on the backside. During SLV deposition very long nanowires with almost monocrystalline internal order formed on the interdigital electrodes, forming networks of randomly interconnected nanowires, as shown in Figure 1a,b.

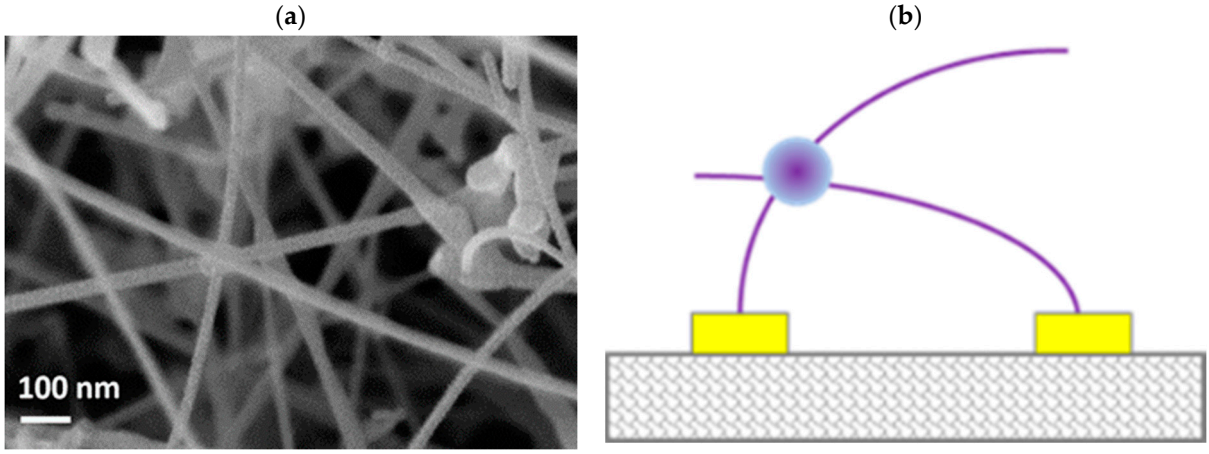

Figure 1. (**a**) SLV-deposited SnO_2 nanowire array, (**b**) current flow across nanowire network.

In order to assess the effects of long-term sensor drift, the nanowires were continually heated to temperatures of 400 °C while being exposed to humidified synthetic air with a relative humidity of $r.h. = 50\%$ at 20 °C. Eventual changes in baseline resistance and gas response were assessed by repeatedly performing CO gas sensing tests as detailed in Appendix A. As shown in Figure 2a, the conductance of the nanowire networks showed a definite trend towards lower conductance both in humidified synthetic air (G_{air}), as well as under CO exposure (G_{CO}). Another interesting observation was that the relative change in conductance under gas exposure, $\Delta G/G = (G_{CO} - G_{air})/G_{air}$, remained relatively constant throughout the entire experiment (Figure 2b).

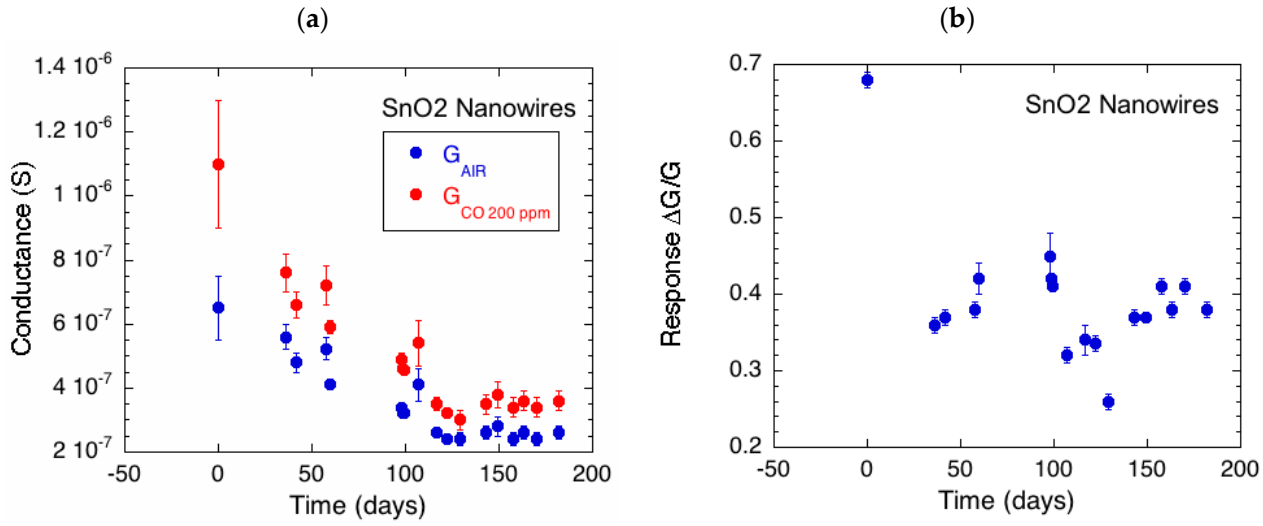

Figure 2. (**a**) Long-term drift in the conductance of SnO_2 nanowire gas sensors exposed to CO (red) and humidified synthetic air (blue); (**b**) relative change in the CO response upon long-term operation.

Upon closing this section, we note that the SLV growth superseded the earlier methods of RGTO (rheotaxial growth and thermal oxidation) growth in the Brescia laboratory [32,33], which consistently produced granular nanocrystalline materials with huge numbers of inter-grain contacts. A surprising result of our investigations was that RGTO materials exhibit very similar degradation characteristics as almost monocrystalline nanowire materials. In order to keep our arguments in this paper reasonably straight and simple, a thorough discussion of RGTO materials, inter-grain contacts and surface band bending regions is deferred to a forthcoming publication [34].

In view of the presently available experimental evidence that similar degradation characteristics can be observed both in fully monocrystalline and in nanogranular materials, we present below an explanation of the phenomenon of sensor baseline drift that focusses entirely on the bulk properties of SnO_2 crystals with nanometric dimensions and with the possibility of efficiently exchanging oxygen between bulk and surface regions.

3. Oxygen Vacancy Donors and Electrical Conductivity in n-Type Metal Oxides

In order to explain the above observations, it is necessary to take a closer look at the intrinsic thermal disorder in the SnO_2 lattice. As is well known, the regular lattice sites in SnO_2 crystals consist of Sn^{4+} and O^{2-} ions, arranged in rutile or cassiterite lattice structures which ensure overall charge neutrality [35–44]. In Kröger–Vink notation [45], the regular lattice sites in SnO_2 crystals are denoted by Sn_{Sn} and O_O, both of which are attributed with zero formal charge. Charge states of more energetic lattice sites, which become possible at higher temperature, are always measured relative to the zero-formal charge of the Sn_{Sn} and O_O lattice sites.

In SnO_2, the most important bulk defect sites are oxygen vacancies V_O which are generated by removing oxygen atoms from regular O_O sites and by injecting the liberated O atoms into the interstitial lattice, thus forming oxygen interstitials O_i. In this process of forming vacancy-interstitial pairs, the two electrons, formerly associated with the O^{2-} lattice ions, remain with the newly formed vacancies. As this negative charge is compensated by the positive ionic charges of the nearest-neighbor Sn ions, both the V_O and the O_i sites maintain zero formal charge. Due to the high mobility of the O_i interstitials, these are able to move towards the free surfaces where they can recombine with other oxygen atoms to form O_2 molecules, which can desorb into the ambient air. O_2 molecules, on the other hand, coming from the air ambient and re-adsorbing on the SnO_2 surface, can break up into individual oxygen atoms and diffuse through the interstitial lattice again until they eventually drop into empty vacancy sites in the interior. Through this exchange of

oxygen across the air–solid interface, an equilibrium concentration of oxygen vacancies will develop inside the crystal, which depends on the temperature T of the crystal lattice and the oxygen partial pressure p_{O_2} in the ambient air. As described in Appendix B, a volume density of oxygen vacancies $N_{VO}(T)$ will then develop, which depends on the volume densities of occupied oxygen ion sites N_O, interstitial vacancy sites N_i, and the vacancy formation energy E_{VO} inside the crystal:

$$N_{VO}(T) = \sqrt{N_O N_i} exp\left[-\frac{E_{VO}}{2k_B T}\right]. \quad (1)$$

Here, E_{VO} is the vacancy formation energy, T—the absolute temperature and k_B—Boltzmann's constant.

The key interest in these vacancy-type defects stems from the fact that these can act as shallow double donors with ionization energies of 30 and 150 meV below the conduction band edge E_C [35–44]. This energetic situation is illustrated in Figure 3a. Shown in Figure 3b is a situation in which the two donor electrons are transferred to a Fermi level E_F lying deeper in the bandgap, from where the two electrons can be re-excited into the conduction band, thus forming mobile charge carriers and enabling electrical conductivity.

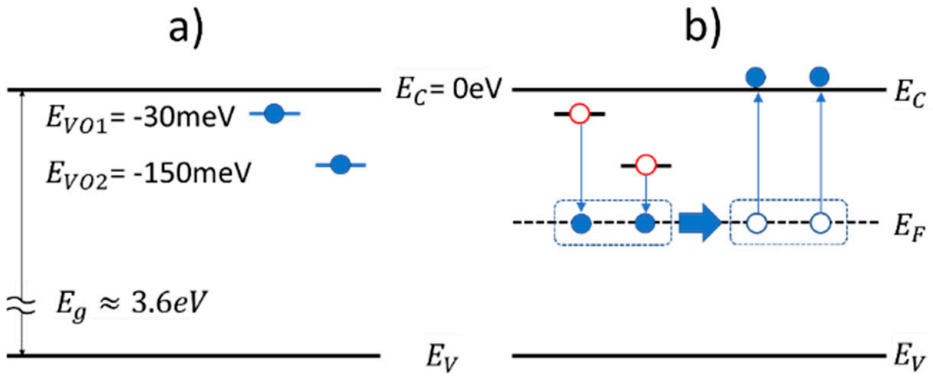

Figure 3. (**a**) Energy levels of oxygen vacancies relative to the conduction and valence band edges in SnO_2; (**b**) transfer of electrons from occupied donor levels to a deeper-lying electron Fermi-energy (left); re-excitation of electrons from the Fermi energy to the conduction band (right).

With the donor levels transferring their electrons to a deeper-lying Fermi energy, the vacancies change their formal charge states from zero to positive and double-positive and they also refund a fraction of their formation energy to the thermal reservoir of lattice vibrations inside the SnO_2 crystal. With these lowered formation energies, the volume densities of singly and doubly ionized vacancy sites are significantly enhanced over the volume density of neutral donor sites and, in particular, the volume densities of these charged vacancies become Fermi-energy-dependent:

$$N_{VO}^{+}(E_F, T) = 2\, N_{VO}(T)\, exp\left[\frac{E_{O_1} - E_F}{k_B T}\right], \text{ and:} \quad (2)$$

$$N_{VO}^{2+}(E_F, T) = N_{VO}(T)\, exp\left[\frac{E_{O_1} - E_F}{k_B T}\right] exp\left[\frac{E_{O_2} - E_F}{k_B T}\right]. \quad (3)$$

In these latter equations E_{O_1} and E_{O_2} stand for the two ionization energies of the double donors. The factor of two in the first equation accounts for the possibility of two different spin orientations inside a singly ionized vacancy. In Appendix B, attention is further drawn to the fact that enhanced densities of oxygen vacancy donors are expected in regions with upward band bending, i.e., near surfaces, at inter-grain contacts and around catalytic metal clusters. These latter effects will be discussed in a follow-on publication [34].

Returning to bulk regions with essentially flat bands, the volume densities of neutral, i.e., fully occupied, singly ionized, and doubly ionized vacancies are plotted in Figure 4a

as a function of the Fermi energy position inside the gap, assuming a lattice temperature of $T \approx 1200$ K, typical of SLV growth conditions and a defect formation energy E_{VO} of 4 eV [46]. Figure 4b, for comparison, shows this same situation, but as evaluated for a much lower temperature of 673 K, which had been chosen as the sensor operation temperature in the long-term tests described in Section 2. Comparing both graphs, it is seen that temperature has a huge influence on the concentration of neutral vacancies but a much more moderate influence on the much larger concentrations of positively charged vacancies with concomitantly lower formation energies. Also shown in Figure 4a,b are the volume densities of mobile electrons that are expected to be re-excited from the respective Fermi energies to the conduction band edge:

$$n(E_F, T) = N_C \, exp\left[-\frac{E_C - E_F(T)}{k_B T}\right]. \tag{4}$$

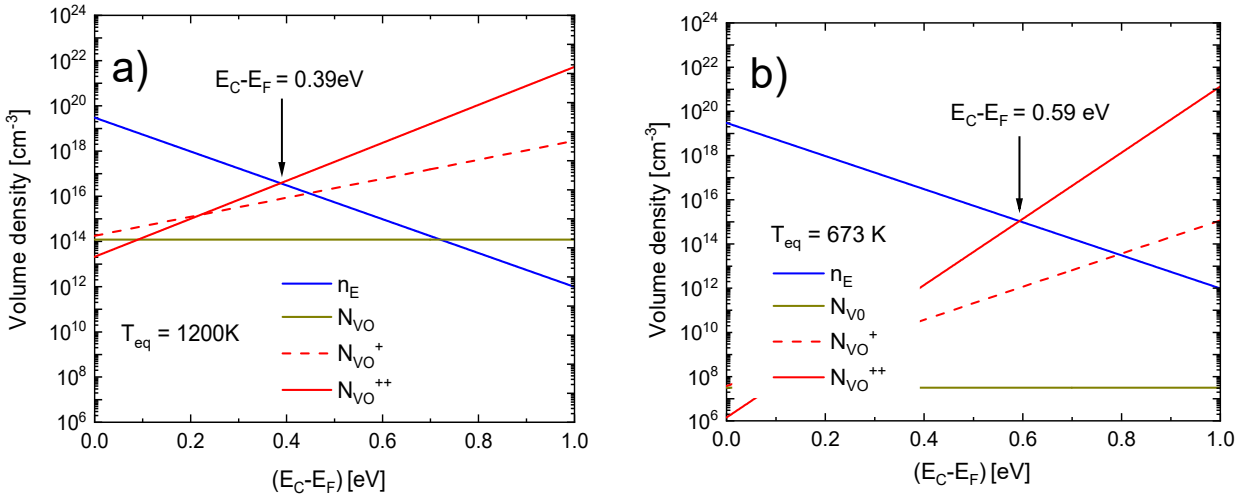

Figure 4. Volume densities of neutral, positively, and twofold positively charged oxygen vacancies as a function of the Fermi-energy inside the forbidden gap (**a**) for a temperature of 1200 K and (**b**) for the chosen sensor operation temperature of 673 K. The blue lines in both sub-figures represent electron concentrations at the conduction band edge.

Comparing both graphs, it becomes evident that the Fermi energy position that ensures overall charge neutrality is mainly determined by the volume densities of electrons and doubly ionized vacancies, i.e.:

$$n(E_F, T) \approx N_{VO}^{2+}(E_F, T). \tag{5}$$

Solving for $E_F(T)$, one then obtains:

$$E_C - E_F(T) = \frac{1}{3}\left\{\frac{E_{VO\_eff}}{2} - k_B \, T \, ln\left[\frac{N_O}{N_C}\right]\right\}, \tag{6}$$

and for the equilibrium charge carrier density:

$$n_{eq}(E_F, T) = N_C^{2/3} N_O^{1/3} \, exp\left[-\frac{E_{VO\_eff}}{6 \, k_B T}\right], \tag{7}$$

with

$$E_{V0\_eff} = E_{V0} + 2(E_C - E_{O_1}) + 2(E_C - E_{O_2}) \tag{8}$$

standing for the effective vacancy formation energy of neutral oxygen vacancies.

Overall, the above equations indicate that in monocrystalline MOX materials an Arrhenius-type temperature-dependence of the electrical conductivity should arise under

thermal equilibrium conditions. Additionally, a fractional power dependence on the volume density of occupied oxygen lattice sites, N_O, should be observed, which depends on the availability of O_2 molecules in the ambient air, i.e., on the oxygen partial pressure p_{O_2} there [35–45]. This dependence on p_{O_2} is widely employed in λ-probes where Ytterbium-doped ZrO_2 crystals are used to measure the difference in oxygen partial pressures in the outside air and exhaust gas streams of automobiles [47]. Due to larger oxygen vacancy formation energies and less mobile oxygen interstitials, these latter effects are less dominant in the electron conductors that are conventionally employed in MOX gas sensors and sensor arrays.

4. Thermal Quenching of Electrical Conductivity and Conductivity Relaxation

So far, our arguments have followed the general background of metal oxide materials widely described and disseminated in the published literature [35–45]. The ideas presented in the following with regard to equilibration, thermal quenching, metastability and sensor drift, in contrast, largely build on ideas previously developed in the field of amorphous semiconductors, and in particular of hydrogenated amorphous silicon (a-Si:H). In order to ease understanding of these issues, some of those ideas are briefly described in Appendix C, where some of the key background literature is also cited.

Considering the fact that the key intrinsic donor defects in MOX materials are oxygen vacancies that can only be formed by simultaneously generating oxygen interstitials, it is clear that adaptations of the donor defect densities to different Fermi energy positions will be kinetically controlled by the rates with which oxygen interstitials are able to diffuse through the interstitial lattices of MOX materials. Upon arriving at one of the free surfaces, pairs of interstitials can recombine into O_2 molecules which are then free to interchange with O_2 molecules in the ambient air, thus allowing the bulk electrical conductivity to equilibrate with the O_2 concentration in the ambient air.

With oxygen diffusion constants $D(T)$ following Arrhenius laws [48–51],

$$D(T) = D_0 \, exp\left[-\frac{E_D}{k_B T}\right], \tag{9}$$

equilibration requires that at each temperature T, the crystal be maintained for a time $\tau_{eq}(T)$ long enough to make the oxygen diffusion length $L_D = \sqrt{D(T)\,\tau_{eq}(T)}$ comparable to the crystal size L_{SnO_2}:

$$L_{SnO_2} = \sqrt{D(T)\,\tau_{eq}(T)}. \tag{10}$$

Combining the latter two equations, $\tau_{eq}(T)$ emerges as:

$$\tau_{eq}(T) = \frac{{L_{SnO_2}}^2}{D_0} exp\left[\frac{E_D}{k_B T}\right]. \tag{11}$$

Considering a situation in which a piece of monocrystalline MOX material is allowed to cool down from the initially very high preparation temperatures to increasingly lower temperatures and that sufficient time is allotted at each temperature to allow equilibration of the oxygen vacancy densities with the outside air, Equation (11) can be inserted in Equation (7) to obtain the equilibrated density of mobile electrons in the conduction band as a function of time:

$$n_{eq}(\,\tau_{eq}) = N_C^{2/3} N_O^{1/3} \, exp\left\{-\frac{1}{6}\frac{E_{VO\_eff}}{E_D}\, ln\left[\frac{D_0\,\tau_{eq}}{{L_{SnO_2}}^2}\right]\right\} \tag{12}$$

In Figure 5, the equilibration temperature T_{eq} reached after a time τ_{eq} is plotted as a function of τ_{eq}. The red line in this plot shows that the SnO_2 lattice will have thermalized to the chosen sensor operation temperature of $T_{MOX} \approx 673$ K after a time $\tau_{eq} \approx 4 \times 10^7$s, corresponding to about 400 days of continuous sensor operation. In this estimate, published

oxygen diffusion parameters [48–51] have been used. The blue line in Figure 5 shows the corresponding drop in the equilibrated charge carrier density after times τ_{eq}. The equilibrium charge carrier density in the conduction band at the chosen sensor operation temperature is then estimated to be about $2 \times 10^{15} \mathrm{cm}^{-3}$, corresponding to an equilibrium bulk conductivity of about $10^{-3} \Omega^{-1} \mathrm{cm}^{-1}$. As shown in Appendix A, such bulk conductivity values are in an order-of-magnitude agreement with the macroscopically determined conductances of $(10^{-7} - 10^{-6})\ \Omega^{-1}$ reported in Figure 2.

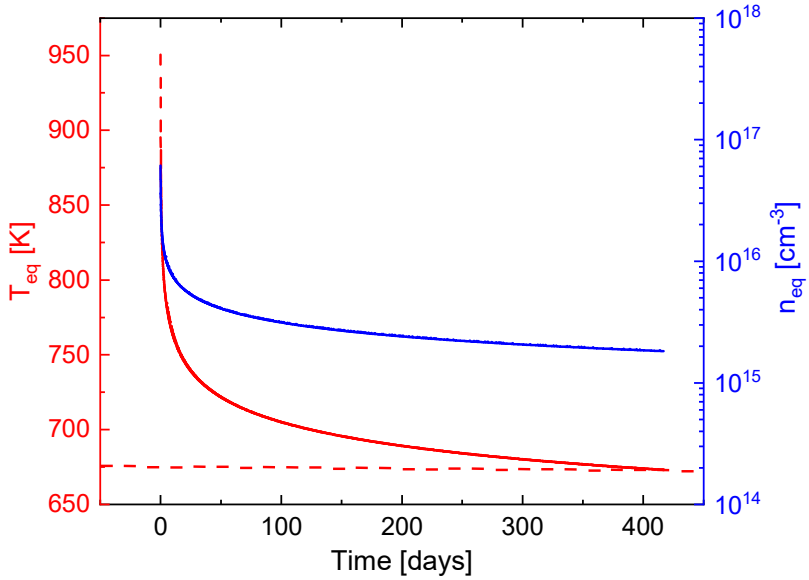

Figure 5. (Red line) Equilibration temperatures reached after times τ_{eq}; (Blue line) equilibrated charge carrier density in the conduction band after times τ_{eq}. Thermal equilibrium at the MOX sensor operation temperature is reached after about $4 \times 10^7 s \approx 400$ days. Up to this point, a considerable drop in the bulk charge carrier density will have occurred.

From both lines in Figure 5, it becomes evident that a considerable part of the equilibration does take place in the initial phases after high-temperature materials preparation and cool-down to storage conditions. During these initial phases of cooldown, the volume density of oxygen vacancy donors rapidly equilibrates to the increasingly lower temperatures until equilibration rates become too slow to allow for further equilibration to continuously lower temperatures. This condition is met after a time τ_{qe}, after which the oxygen vacancy donor density has dropped to an equilibrium value corresponding to a temperature.

$$T_{qe}(\tau_{qe}) = \frac{E_D}{k_B \, ln\left[\frac{D_0 \, \tau_{qe}}{L^2_{SnO_2}}\right]}. \tag{13}$$

Below this temperature, the different kinds of oxygen vacancy densities become frozen in metastable non-equilibrium states whose volume densities do no longer change as temperatures further drop. These latter conditions of initial equilibration and following quench-in are illustrated in Figure 6a,b, with the first figure representing freeze-in of neutral oxygen vacancy donors at different temperatures T_{qe} and the second freeze-in of twofold positively charged oxygen vacancy donors at these same temperatures T_{qe}.

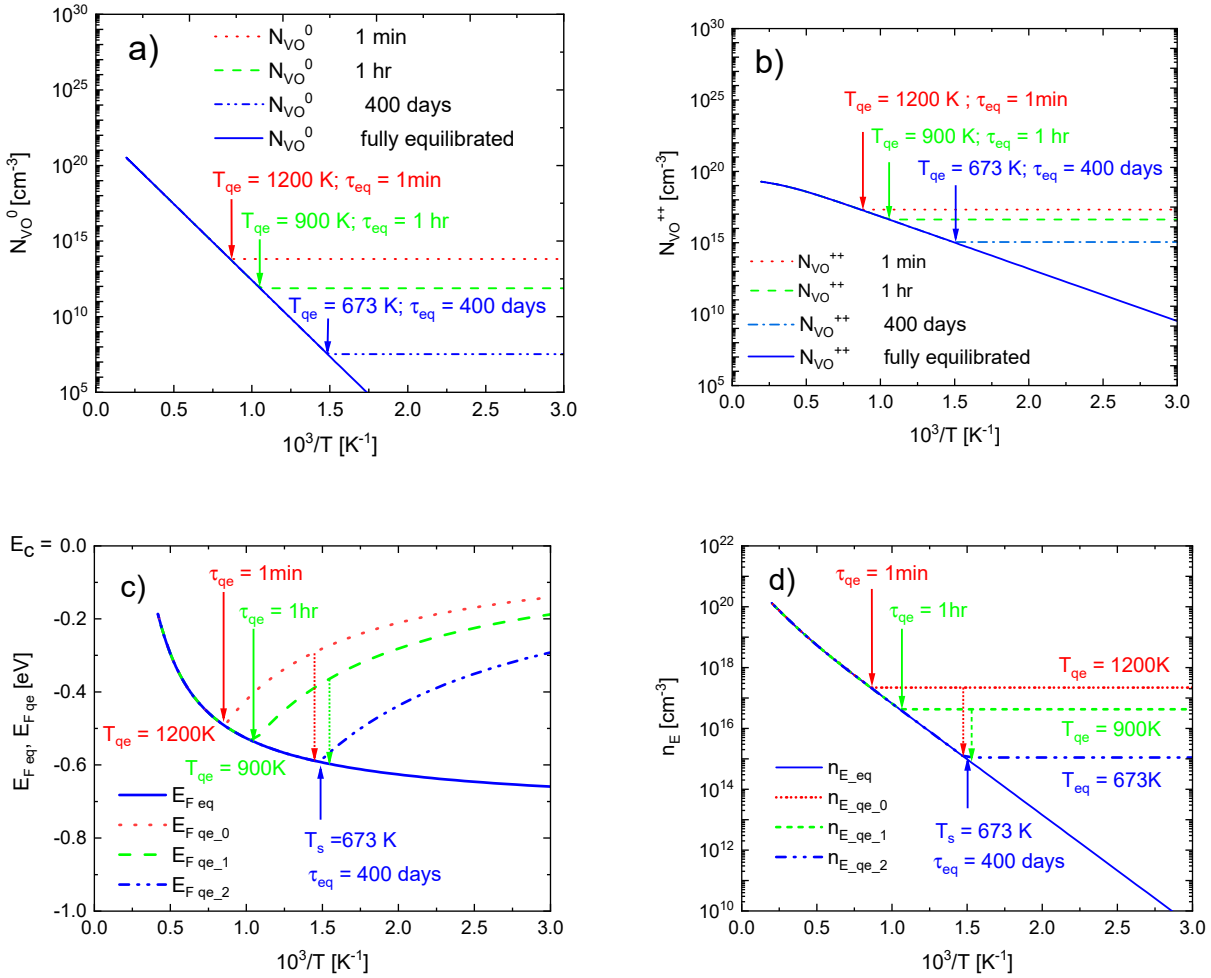

Figure 6. (**a**,**b**): Effect of increasingly longer equilibration times τ_{eq} on the quenched-in (qe) concentrations of neutral (**a**) and two-fold positively charged (**b**) oxygen vacancy densities. Quenched-in concentrations relate to increasingly lower quench-in temperatures T_{qe}; (**c**,**d**): Effect of thermal quenching on temperature-dependent Fermi energy positions (**c**) and quenched-in excess carrier densities (**d**). Dash-dotted vertical lines indicate slow subsequent relaxation towards sensor operation temperature specific values of Fermi energy position and equilibrated mobile carrier densities.

The two bottom pictures of Figure 6 show the consequences that arise for the quenched-in non-equilibrium states with regard to the temperature-dependent Fermi level positions (Figure 6c) and mobile electron densities in the conduction band (Figure 6d). Both pictures show that MOX materials in their quenched-in states behave like "normal" semiconductors doped with substitutional n-type donor impurities. In these quenched-in states, Fermi energies are very close to the conduction band at very low temperatures and shift down deeper into the forbidden gap due to the effects of statistical Fermi energy shift as temperatures are increased [40]. In these states, the concomitant effects of increasingly larger activation energies for mobile charge carrier excitation are counteracted by the exponentially increasing probabilities of mobile charge carrier generation as temperatures increase. In this way, temperature-independent densities of mobile charge carriers arise in these quenched-in metastable states. When temperatures are increased towards and beyond the initial quench-in temperature T_{qe_1}, the quenched-in metastable states again become unstable and start to rapidly equilibrate again. While equilibration is relatively fast at and around the originally employed quench-in temperature T_{qe_1}, the quenched-in metastable states are also unstable at much lower temperatures. At temperatures $T < T_{eq\_1}$, however, the rates of relaxation towards equilibrium are much longer than usually employed changes in gas concentration, sensor operation or biasing conditions [52,53]. Equilibration in these latter cases usually

goes undetected and only shines up when specifically designed long-term tests are carried out, as described in Section 2.

Returning to the problem of analyzing experimental sensor drift data, one problem is that in such analyses, neither times nor temperatures of freeze-in are known. In this situation, the best approach is returning to Equation (12) and evaluating the ratio of conductivities at the beginning and at all intermediate times during the long-term stability tests. In this way, the loss in sensor conductivity $\sigma_{loss}\left(\tau, \tau_{ref}\right)$ at time τ can be related to the unknown reference time τ_{ref} at which the metastable state of concern had been quenched-in:

$$\sigma_{loss}\left(\tau, \tau_{ref}\right) = \frac{n_{eq}(\tau)}{n_{eq}\left(\tau_{ref}\right)} = exp\left\{-\frac{1}{6}\frac{E_{VO\_eff}}{E_D}\, ln\left[\frac{\tau}{\tau_{ref}}\right]\right\}. \quad (14)$$

With the bulk values of the vacancy formation energy $E_{VO\_eff} \approx 4$ eV [46], and an oxygen diffusion energy $E_D \approx 1.83$ eV, well within the range of published oxygen diffusion data [48–51], the data in Figure 7 were obtained. The only free parameter in this equation is the reference time $\tau_{ref} \approx 10^6$ s ≈ 6 d. This latter figure indicates that some uncontrolled equilibration may have taken place either during cool-down from preparation or during some initial gas-sensing tests prior to initiating the very long-term tests.

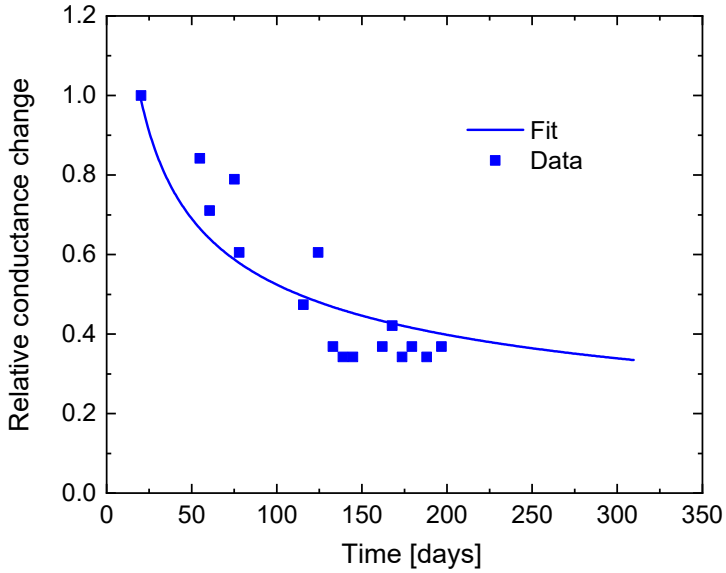

Figure 7. Decrease in baseline conductivity upon slow relaxation from quenched-in non-equilibrium states towards equilibrium states corresponding to the sensor operation temperature of 673 K applied in the experiments described in Section 2: Full line: calculated from Equation (14) assuming bulk conductivity limitation; data points: Brescia long-term sensing test (Section 2).

The other interesting piece of experimental evidence presented in Section 2 is the parallel variation of the relative gas response upon prolonged sensor operation. Such parallel variations in sensor baseline conductance and relative gas response had already been observed in earlier experiments and explained in references [41,42]. This subject will also be taken up again in our forthcoming publication dealing with surface band bending regions [34].

5. Impurity Doping, Mitigation and Suppression of Sensor Drift

So far, we have been dealing with the intrinsic oxygen vacancy donors which turn many MOX materials naturally n-type. As a culmination point, we have arrived at the conclusion that the experimentally observed effects of sensor drift arise from the slow

annealing of quenched-in oxygen vacancy donors. In this final section, we turn to n-type and p-type doping by adding metal impurities with chemical valences different from those of the core metal constituents of the host crystals. These latter considerations reveal that the formation of positively ionized oxygen vacancy donors can be largely suppressed, and sensor drift effects be mitigated by adding n-type impurities whose densities are permanently fixed during materials preparation. P-type doping, in contrast, appears less attractive as it enhances the formation of oxygen vacancy donors which are responsible for the sensor drift.

Dissimilar to crystalline silicon (c-Si), for instance, where both heavy n- and p-type impurity doping is possible, a large asymmetry between n- and p-type doping exists in n-type metal oxides. This asymmetry is illustrated in Figure 8. Figure 8a shows that incorporating increasing densities of donor impurities successfully moves the Fermi energy from its intrinsic position in the upper half of the forbidden gap to positions increasingly closer to the conduction band. As in c-Si and other crystalline semiconductors, largely enhanced and temperature-independent mobile electron densities are then observed (Figure 8b). Similar to conventional semiconductors, the introduction of increasing densities of acceptor impurities does move the Fermi energy deeper into the forbidden gap, a conversion towards p-type conductivity, however, cannot be observed in this case. This latter fact is vividly demonstrated by Figure 8b, where it is shown that Arrhenius-type temperature dependencies, similar to the undoped case, are retained. Any signs of an extrinsic and temperature-independent p-type conductivity, however, clearly do not show up.

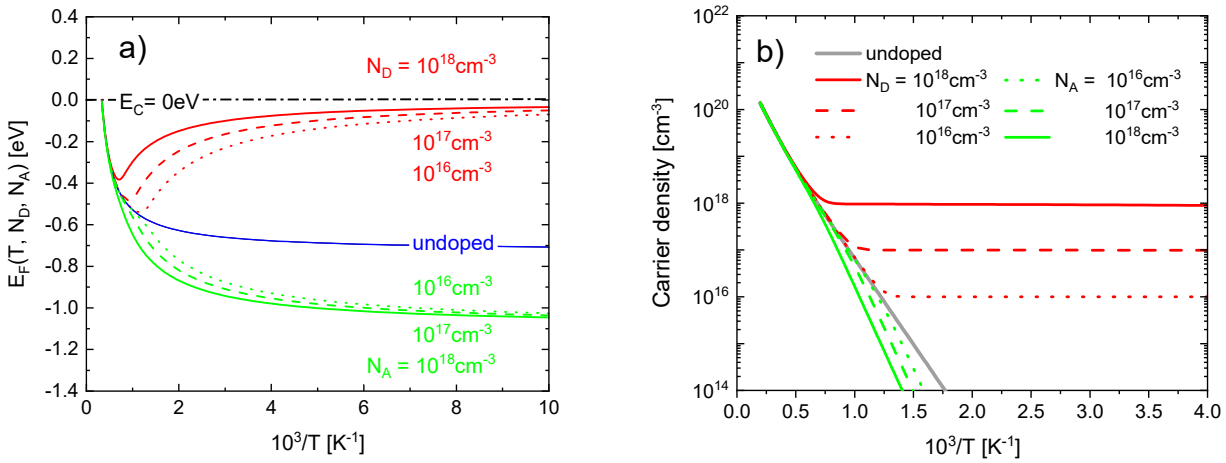

Figure 8. (**a**) Effect of n- and p-type impurity doping on Fermi energy position within the forbidden gap, and (**b**) on mobile charge carrier concentrations.

The observed asymmetry of n- and p-type doping is a direct consequence of Equations (2) and (3), which predict that oxygen vacancy concentrations are Fermi-energy-dependent. While the introduction of shallow n-type donors prevents neutral oxygen vacancies from discharging towards singly and doubly ionized positive charge states, Figure 9a shows that in this case, the densities of positively charged oxygen vacancies are hardly able to equilibrate to densities much higher than the neutral donor density. Similar to conventional semiconductors, the electroneutrality condition in n-type doped MOX materials is then dominated by the equation $n_{E\_n} \approx N_D^+$, where N_D is the donor impurity density and n_{E_n} the mobile electron density in n-type doped material. Considering the fact that the concentration of donor impurities N_D is permanently fixed during materials preparation, the baseline conductivity and its ensuing gas response become independent of the lattice temperature. Sensor drift thus can be mitigated or even suppressed. In this context, it is relevant to note that n-type doping of SnO_2, for instance, is possible by substituting antimony ions on Sn_{Sn} lattice sites in SnO_2 [52].

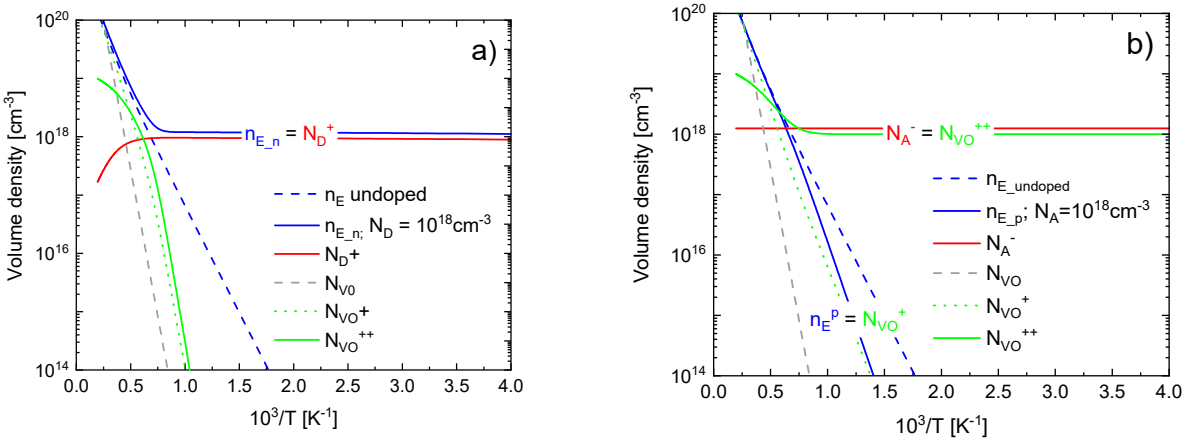

Figure 9. Effect of n-type (**a**) and p-type impurity doping (**b**) on mobile electron density and densities of the differently charged oxygen vacancy centers. Electron and positive donor densities in (**a**) and negative acceptor and twofold positive vacancy densities in (**b**) have been slightly displaced from their positive counterparts for clarity of presentation.

The situation of p-type doping with shallow acceptor impurities is a very different one. In this case, empty acceptors with energy levels close to the valence band edge, actively drive neutral oxygen vacancies towards their positively charged states and densities of N_{VO}^{++} donor sites towards high and acceptor-controlled densities satisfying $N_{VO}^{++} \approx N_A^-$. Figure 9b shows that in this case, the Fermi energy is pinned between equal densities of positively charged vacancy donor levels close to the conduction band edge and negatively charged acceptor impurity levels close to the valence band edge. The small remaining mobile electron densities n_{E_p} in this case are counterbalanced by similarly small and very strongly temperature-dependent densities of singly charged N_{VO}^+ vacancies, i.e., $n_{E\_p} \approx N_{VO}^+$. As the densities of N_{VO}^+ sites remain sensitive to the lattice temperature, doping with p-type impurities does not appear to be an equally interesting option, as n-type impurity doping for mitigating or suppressing sensor drift.

In concluding this section, we note that similar effects of sensor baseline drift and ensuing changes in gas response as in Section 2 have also been observed in p-type NiO [31]. It therefore appears that our arguments can—mutatis mutandis—also be extended to p-type materials. In brief, it appears possible that intrinsically p-type materials can be stabilized by p-type impurity doping thus overwhelming the effects of intrinsic metal vacancies.

6. Conclusions

In this paper, we have provided experimental evidence for the effect of sensor baseline resistance drift in metal oxides, and we have developed a framework for the theoretical explanation of this effect.

Concerning experimental evidence, we have concentrated on SnO_2 as the most extensively used MOX material for resistive gas sensors. Performing tests on SLV-deposited nanowire materials, we have provided evidence that sensor drift is not an artifact arising from poor crystallinity, but that the phenomenon of sensor drift principally also occurs in materials with almost ideal crystalline order.

Building on the fact that the nanowire materials had not been intentionally doped with metal impurities with chemical valences different than the core Sn ions, a theoretical framework has been developed which focuses on shallow oxygen-vacancy donors as the key reason for the occurrence of sensor baseline drift.

With shallow oxygen vacancy donors being key components of the thermal lattice disorder, their number densities are principally dependent on the sensor operation temperatures that are being employed. As oxygen vacancy donors can exist in three different charge states, i.e., neutral, singly and doubly positively charged, their charge states and number densities are also sensitively dependent on Fermi-level positions in the sensor´s bulk and

at band-bending regions at the nanowire surfaces. Whereas annealing of quenched-in bulk vacancy donors cause the sensor baseline conductivity to drop, the annealing of vacancy donors also lowers the capability of the nanowires to adsorb surface oxygen ions. In this way, concomitant changes towards lower reducing gas responses are initiated. These latter conclusions about adsorption are still of a preliminary nature and more detailed results will be reported in a follow-on publication which will deal in an exhaustive manner with the effects of adsorption, band bending, and equilibration processes in nanowires and granular materials with large numbers of inter-grain contacts [34].

As equilibration rates of oxygen vacancy donors are limited by the slow rates of diffusion of lattice oxygen ions, equilibration processes normally do not become visible at the relatively fast rates at which gas exposure conditions and sensor operation parameters are being changed [53,54]. Due to the low speed of defect equilibration processes, the effects of long-term sensor drift often take the form of apparently random and hardly reproducible dirt effects. With the approaches taken in this paper, a framework has been established that allows such seemingly irreproducible effects to be turned into reproducible effects that are amenable to physical analysis.

As authors, we regard our experiments and theoretical treatments as a first step towards more systematic investigations of sensor drift effects and their impacts on gas sensitivity changes and gas discrimination capabilities of metal oxide materials. The potential reward of baseline resistance suppression discussed in Section 5 appears to be a good motivation to progress towards this direction.

Author Contributions: Conceptualization and original draft preparation, G.M., materials preparation, long-term sensor performance tests and experimental data procurement G.S. All authors have read and agreed to the published version of the manuscript.

Funding: Project NMP- 7FP: Surface ionization and novel concepts in nano-MOX gas sensors with increased Selectivity, Sensitivity and Stability for detection of low concentrations of toxic and explosive agents. Contract number 247768 Coordinator Prof Giorgio Sberveglieri CNR—INFM project budget 469.000,00 Euro.

Institutional Review Board Statement: Not applicable.

Informed Consent Statement: Not Applicable.

Data Availability Statement: Not Applicable.

Conflicts of Interest: The authors declare no conflict of interest. The funders had no role in the design of the study; in the collection, analyses, or interpretation of data; in the writing of the manuscript, or in the decision to publish the results.

Appendix A. Materials Preparation and Long-Term Tests

SnO_2 nanowires were prepared by the solid–liquid–vapor (SLV) condensation technique. SnO_2 material was placed in the high-temperature zone of a cylindrical quartz tube and transported by an argon gas stream towards a ceramic substrate with pre-deposited platinum electrodes and condensed there in single-crystal nanowire form. Nanowires with lengths up to several hundred μm and thicknesses in the order of 100 nm then formed on the Pt interdigital electrodes (IDE) thus forming "spaghetti-type" networks with random inter-wire contacts thus bridging the IDE gaps [30,31]. The resulting electrical arrangements are schematically illustrated in Figure A1a,b. With the bulk conductivities reported in Figure 5, single nanowires with cross sections in the order of 100 nm are expected to exhibit resistances in the order of $10^{11}\Omega$. The macroscopically observed resistances in the order of (10^6–10^7) Ω imply parallel connections of (10^4–10^5) nanowires, i.e., nucleation densities of nanowires in the order of (0.1–1) μm^{-1}, as illustrated in Figure A1b and as similarly indicated in Figure 1a.

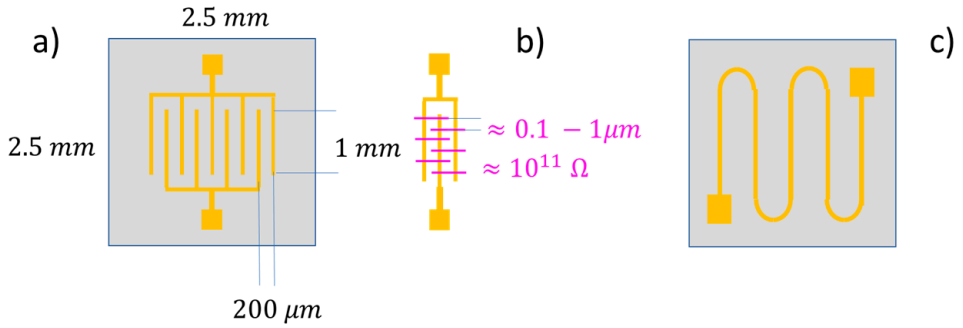

Figure A1. Electrical readout of SLV-deposited SnO_2 nanowires: (**a**) Interdigital Pt electrodes; (**b**) SnO_2 nanowires bridging Pt electrodes; (**c**) back-surface Pt heater meander.

After preparation, both types of materials were operated for prolonged periods of time at a constant temperature of 400 °C, and repeatedly tested for their CO response following the protocol displayed in Figure A2.

Sensors:
SnO_2 nanowires
SnO_2 RGTO
Sensor T = 400 °C
Baseline atmosphere:
Wet air, r.h. = 50% at 20 °C
Target gas: CO
(no surface poisoning)

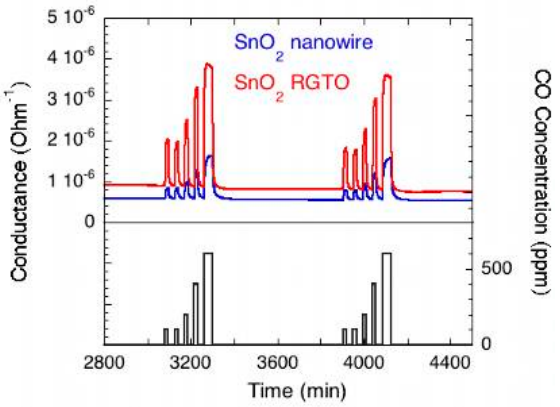

Figure A2. Test protocol employed to assess the long-term performance of SLV and RGTO-deposited SnO_2 materials.

Appendix B. Oxygen Vacancies as Elements of Thermal Disorder in MOX Materials

In the main part of this paper, our focus has been on SnO_2 as one of the key materials used in resistive MOX gas sensors. As we believe that the arguments presented above will have a much wider range of applicability beyond SnO_2, the key Equations (1)–(3) in the main text will be rederived from elementary considerations about a simplified and idealized form of MOX material. The model substance considered is a two-dimensional lattice consisting of positive metal ions and negatively charged oxygen ions. The equations below largely follow the lines of thought presented in the textbook of O. Madelung [44].

In Figure A3, the positive background of metal ions is represented by a homogenous background of positive charge with discrete negative oxygen ions embedded into this jellium of positive charge. While Figure A3a represents the ideal case of complete order that is principally accessible at the absolute zero of temperature, Figure A3b represents a state that is more likely to arise when the crystal lattice is operated at finite temperature. In this latter picture, a situation is shown in which three oxygen vacancy-interstitial pairs are distributed across the available oxygen (O_O) and interstitial (O_i) sites.

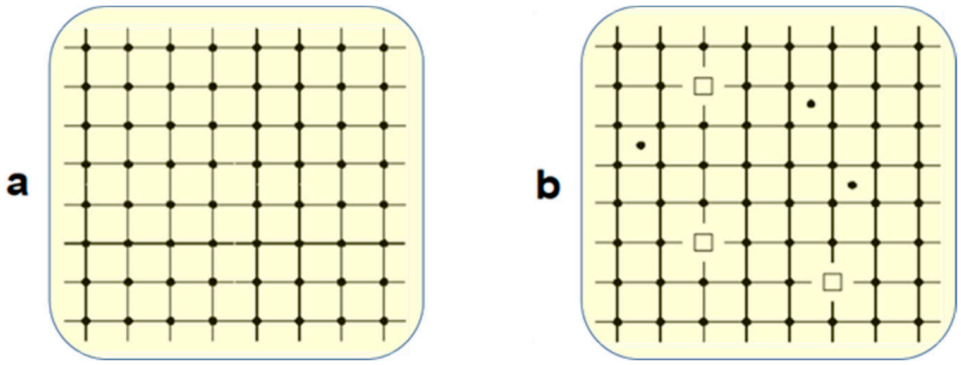

Figure A3. Simplified model of a MOX crystal of (**a**) without and (**b**) with thermal disorder. The thermally disordered crystal features three vacancy-interstitial pairs, resulting in an enlarged free energy $\Delta F = \Delta E - T\Delta S$.

Generating such vacancy-interstitial pairs requires energies E_{VO} per vacancy-interstitial pair and an amount of energy

$$\Delta E = N_{VO} E_{VO} \tag{A1}$$

when N_{VO} of such pairs are created. As such pairs can be distributed across the available O_O and O_i sites, an entropy ΔS is associated with the generation of these vacancies:

$$\Delta S = k_B ln\left[\frac{N_O!}{N_{VO}!(N_O - N_{VO})!}\,\frac{N_i!}{n_i!(N_i - n_i)!}\right]. \tag{A2}$$

In this latter equation, N_O and N_i stand for the numbers of available O_O and O_i sites and N_{VO} and n_i for the numbers of vacancies and interstitials that have actually been formed.

In order to obtain the equilibrium concentration of oxygen vacancies at a fixed temperature T, the free energy

$$\Delta F = \Delta E - T\Delta S \tag{A3}$$

needs to be minimized. With the requirement $d(\Delta F)/d(N_{VO}) = 0$ and the use of Stirling´s formula ($\ln(n!) = n\,ln(n) - n$), Equation (1) of the main text is obtained:

$$N_{VO}(T) = \sqrt{N_O\,N_i}\,exp\left[-\frac{E_{VO}}{2\,k_B T}\right]. \tag{A4}$$

Re-writing Equation (A4) in the form

$$\frac{(N_O - n_i)(N_i - n_i)}{n_i^2} = exp\left[-\frac{E_{VO}}{k_B T}\right], \tag{A5}$$

it emerges that Equation (A5) can be interpreted as a law of mass action connecting the different kinds of lattice and defect sites:

occupied lattice site + unoccupied interstitial site <—->

<—-> unoccupied lattice site + occupied interstitial site.

Further assuming $N_O = N_i$, Equation (A4) reduces to:

$$N_{VO}(T) = N_O\,exp\left[-\frac{E_{VO}}{2\,k_B T}\right]. \tag{A6}$$

From Equation (A4), the number densities of positively charged oxygen vacancy donor sites (Equations (2) and (3) of the main text) follow:

$$N_{VO}^{+}(E_F, T) = 2\, N_{VO}(T)\, exp\left[\frac{E_{O1} - E_F}{k_B T}\right], \text{ and:} \tag{A7}$$

$$N_{VO}^{2+}(E_F, T) = N_{VO}(T)\, exp\left[\frac{E_{O1} - E_F}{k_B T}\right] exp\left[\frac{E_{O_2} - E_F}{k_B T}\right]. \tag{A8}$$

In regions with upward band-bending profiles $q\varphi(x)$, the generation of positively charged oxygen vacancy donors benefits from additional position-sensitive energy gains:

$$N_{VO}^{+}(E_F, T, x) = N_{VO}^{+}(E_F, T)\, exp\left[\frac{q\varphi(x)}{k_B T}\right], \text{ and:} \tag{A9}$$

$$N_{VO}^{2+}(E_F, T, x) = N_{VO}^{2+}(E_F, T)\, exp\left[\frac{2\, q\varphi(x)}{k_B T}\right]. \tag{A10}$$

In such events, higher oxygen vacancy donor densities and higher levels of oxygen depletion are expected to arise as bands continually bend up. These latter effects will be discussed in a forthcoming publication [34]. There, we will deal with the coordinated effects of surface band bending, surface oxygen adsorption and sub-surface oxygen depletion and associated effects of sensor drift.

Appendix C. Electronically Induced Metastability and Drift in Amorphous Semiconductors

While the equations in Appendix B build on the general background of MOX materials widely described and disseminated in the published literature [35–45], the ideas about doping, equilibration, metastability and drift in MOX materials described in the main text have largely developed during the extensive work that had previously been performed in the field of amorphous semiconductors, and, in particular, on hydrogenated amorphous silicon (a-Si:H) [55–61]. For the convenience of the reader, the key ideas of electronically driven weak bond-dangling bond conversion, bond separation and stabilization processes via hydrogen diffusion are pictorially presented in Figures A4–A7. The illustrated microscopic processes have successfully explained the multitude of photo-, doping- and bias-induced defect formation, equilibration and drift processes that had been observed in amorphous semiconductor films and devices. In brief: while the weak bond—dangling bond equilibria are determined by the availability of electrons and holes, i.e., by the positions of Fermi and quasi-Fermi energies, the speeds at which weak-bond dangling bond equilibria can adapt to changes in Fermi- or quasi-Fermi level positions are kinetically controlled by the rates of H-diffusion. Whereas equilibration is fast at elevated temperature (T~200 °C) where bonded hydrogen is reasonably mobile, equilibration is slow at room temperature. Upon rapid cooling from elevated temperatures towards room temperature, high-temperature equilibria thus turn into "frozen in" metastable non-equilibrium states, which slowly relax towards their new room temperature equilibria. A-Si:H device properties, therefore, are subject to drift. Ultimately, these ideas on a-Si:H had all been consolidated by the Xerox group in the so-called "Hydrogen glass model" which is excellently reviewed in the textbook of R.A. Street [61].

Regarding the above processes, it is relevant to note that overall equilibria between electronic and lattice subsystems are by no means limited to disordered materials. Overall equilibria between electronic charge carriers and charged defect centers can principally arise in all kinds of solids as such equilibria are driven by the universal principle of charge conservation and the requirement of overall charge neutrality on macroscopic scales. In particular, such electronically driven equilibria exist in crystalline MOX materials and amorphous semiconductors alike. Material-specific differences arise according to the microscopic nature of the defects and the kinds of kinetic constraints that limit the speed of equilibration inside the individual materials. Whereas overall equilibria between

mobile charge carriers and charged lattice defects are well appreciated in the field of MOX materials [35–45], the related issues of thermal quenching, metastability and drift arising out of the limited and temperature-dependent speeds of oxygen diffusion have attracted much less attention in gas-sensitive and electron-conducting MOX materials [62]. Considering the fact that much larger backgrounds of knowledge about quenching, metastability and drift had emerged in the field of amorphous semiconductors, a cross-fertilization between different fields of materials science appears possible with the possible benefit of valuable new insights into MOX materials.

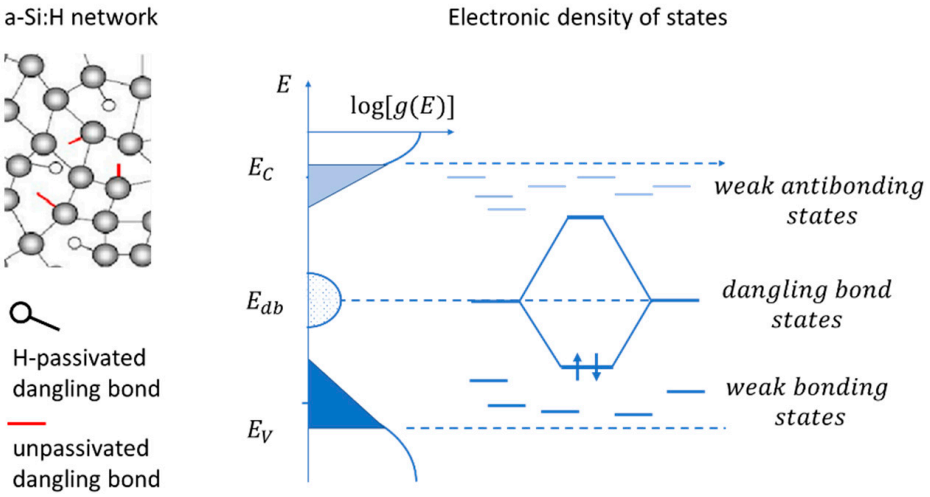

Figure A4. Mechanical strain on Si-Si nearest neighbor bonds reduces the bonding–antibonding gap and causes conduction and valence band states to become localized into exponential conduction and valence band tails (triangular areas). Depending on electron (hole) availability, weak bonds can decay into pairs of dangling bonds with localized states near mid-gap.

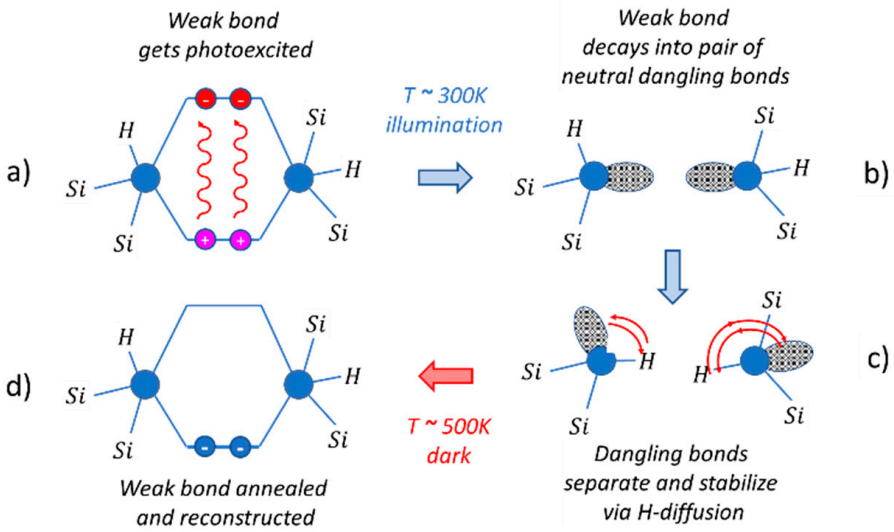

Figure A5. (**a**) Photo-dissociation of weak bonds (Staebler–Wronski effect [57]) into pairs of neutral dangling bonds (**b**) which separate via H-diffusion (**c**). Separated dangling bonds are metastable at room temperature (**c**). In darkness, weak bonds can reform at elevated temperatures and under conditions of enhanced H-mobility (**d**).

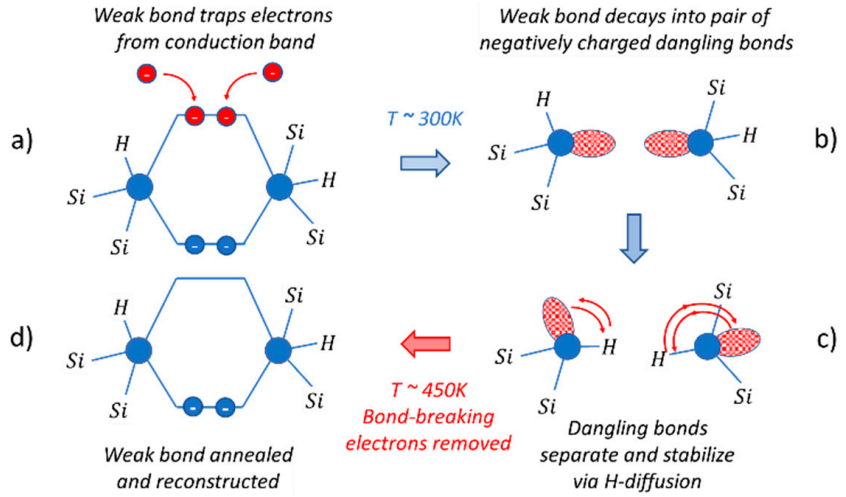

Figure A6. (**a**) Electrons supplied by shallow donors, injected through contacts or induced by field effect become trapped in weak antibonding states and cause weak bonds to convert in pairs of negatively charged dangling bonds (**b**) [56,57]. Dangling bonds are once again separated and stabilized via H-diffusion forming metastable conduction states (**c**). At room temperature, metastable conduction states slowly relax after the bond-breaking electrons have disappeared (**d**) [60,61].

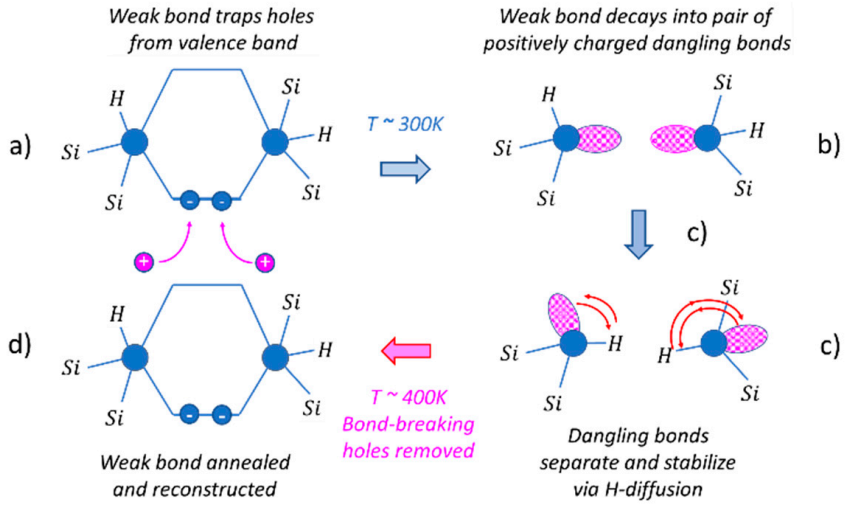

Figure A7. Same as in Figure A6 but with excess holes taking the roles of bond-breaking charges. In this case pairs of positively charged dangling bond defects are formed which are separated and stabilized via H-diffusion.

References

1. Gardner, J.W.; Bartlett, P.N. *Electronic Noses: Principles and Application*; Oxford University Press: Oxford, UK, 1999; ISBN 0-19-855955-0.
2. Jaeschke, C.; Gonzalez, O.; Padilla, M.; Richardson, K.; Glöckler, J.; Mitrovics, J.; Mizaikoff, B. A Novel Modular System for Breath Analysis Using Temperature Modulated MOX Sensors. *Proceedings* **2019**, *14*, 49. [CrossRef]
3. Danesh, E.; Dudeney, R.; Tsang, J.-H.; Blackman, C.; Covington, J.; Smith, P.; Saffell, J. A Multi-MOx Sensor Approach to Measure Oxidizing and Reducing Gases. *Proceedings* **2019**, *14*, 50. [CrossRef]
4. Shaposhnik, A.; Moskalev, P.; Vasiliev, A. Selective Detection of Hydrogen and Hydrogen Containing Gases with Metal Oxide Gas Sensor Operating in Non-Stationary Thermal Regime. *Proceedings* **2019**, *14*, 2. [CrossRef]
5. Byun, H.-G.; Yu, J.-B.; Kang, C.-Y.; Jang, B.K.; Lee, H.-R. Comparative Analysis between Blood Test and Breath Analysis Using sensors Array for Diabetic Patients. *Proceedings* **2019**, *14*, 22. [CrossRef]
6. Astolfi, M.; Zonta, G.; Landini, N.; Gherardi, S.; Rispoli, G.; Anania, G.; Benedusi, M.; Guidi, V.; Palmonari, C.; Secchiero, P.; et al. Chemoresistive Nanostructured sensors for Tumor Pre-Screening. *Proceedings* **2019**, *14*, 29. [CrossRef]
7. Abbatangelo, M.; Duina, G.; Comini, E.; Sberveglieri, G. MOX sensors to Ensure Suitable Parameters of Grated Parmigiano Reggiano Cheese. *Proceedings* **2019**, *14*, 38. [CrossRef]

8. Izawa, K. SnO_2-Based Gas Sensor for Detection of Refrigerant Gases. *Proceedings* **2019**, *14*, 32. [CrossRef]
9. Portalo-Calero, F.; Lozano, J.; Meléndez, F.; Arroyo, P.; Suárez, J.I. Identification of Poisonous Mushrooms by Means of a Hand-Held Electronic Nose. *Proceedings* **2019**, *14*, 33. [CrossRef]
10. Landini, N.; Anania, G.; Astolfi, M.; Fabbri, B.; Gaiardo, A.; Gherardi, S.; Giberti, A.; Guidi, V.; Rispoli, G.; Scagliarini, L.; et al. Nanostructured Chemoresistive sensors for Oncological Screening: Preliminary Study with Single Sensor Approach on Human Blood Samples. *Proceedings* **2019**, *14*, 34. [CrossRef]
11. Zonta, G.; Astolfi, M.; Gaiardo, A.; Gherardi, S.; Giberti, A.; Guidi, V.; Landini, N.; Malagù, C. Semiconductor Gas sensors to Analyze Fecal Exhalation as a Method for Colorectal Cancer Screening. *Proceedings* **2019**, *14*, 35. [CrossRef]
12. Reidt, U.; Helwig, A.; Müller, G.; Lenic, J.; Grosser, J.; Fetter, V.; Kornienko, A.; Kharin, S.; Novikova, N.; Hummel, T. Detection of Microorganisms with an Electronic Nose for Application under Microgravity Conditions. *Gravit. Space Res.* **2020**, *8*, 1–17. [CrossRef]
13. Reidt, U.; Helwig, A.; Müller, G.; Plobner, L.; Lugmayr, V.; Kharin, S.; Smirnov, Y.; Novikova, N.; Lenic, J.; Fetter, V.; et al. Detection of Microorganisms Onboard the International Space Station Using an Electronic Nose. *Gravit. Space Res.* **2017**, *5*, 89–111. [CrossRef]
14. Helwig, A.; Müller, G.; Wassner, T.; Eickhoff, M.; Sberveglieri, G.; Faglia, G. Analysis of the baseline drift phenomenon in nano crystalline SnO_2 gas sensing layers. In Proceedings of the 11th International Meeting on Chemical Sensors, Brescia, Italy, 16–19 July 2006; Available online: https://www.researchgate.net/publication/259361252_Analysis_of_the_baseline_drift_phenomenon_in_nano-crystalline_SnO2_gas_sensing_layers (accessed on 13 March 2022).
15. S3 Project: FP7-NMP-2009-EU-Russia: Surface Ionization and Novel Concepts in Nano-MOX Gas sensors with Increased Selectivity, Sensitivity and Stability for Detection of Low Concentrations of Toxic and Explosive Agents. Contract Number 247768. Available online: https://cordis.europa.eu/project/id/247768/de (accessed on 1 May 2022).
16. Korotcenkov, G.; Cho, B. Instability of metal oxide-based conductometric gas sensors and approaches to stability improvement (short survey). *Sens. Actuators B Chem.* **2011**, *156*, 527–538. [CrossRef]
17. Hrichi, S.; Chaabane-Banaoues, R.; Bayar, S.; Flamini, G.; Oulad El Majdoub, Y.; Mangraviti, D.; Mondello, L.; El Mzoughi, R.; Babba, H.; Mighri, Z.; et al. Botanical and Genetic Identification Followed by Investigation of Chemical Composition and Biological Activities on the *Scabiosa atropurpurea* L. Stem from Tunisian Flora. *Molecules* **2020**, *25*, 5032. [CrossRef] [PubMed]
18. Beer, S. *Personal Communication*; University of Freiburg: Freiburg, Germany, 28 March 2012.
19. Holmberg, M.; Winquist, F.; Lundström, I.; Davide, F.; DiNatale, C.; D'Amico, A. Drift counteraction for an electronic nose. *Sens. Actuators B Chem.* **1996**, *36*, 528–535. [CrossRef]
20. Artursson, T.; Ekl, T.; Lundström, I.; Martensson, P.; Sjöström, M.; Holmberg, M. Drift correction for gas sensors using multivariate methods. *J. Chemom.* **2000**, *14*, 711–723. [CrossRef]
21. Ziyatdinov, A.; Marco, S.; Chaudry, A.; Persaud, K.; Caminal, P.; Perera, A. Drift compensation of gas sensor array data by common principal component analysis. *Sens. Actuators B Chem.* **2010**, *146*, 460–465. [CrossRef]
22. Vergara, A.; Vembu, S.; Ayhan, T.; Ryan, M.A.; Homer, M.L.; Huerta, R. Chemical gas sensor drift compensation using classifier ensembles. *Sens. Actuators B Chem.* **2012**, *166–167*, 320–329. [CrossRef]
23. Abidin, M.Z.; Asmat, A.; Hamidon, M.N. Identification of initial drift in semiconductor gas sensors caused by temperature variation. In Proceedings of the IEEE 9th International Colloquium on Signal Processing and its Applications, Kuala Lumpur, Malaysia, 8–10 March 2013; pp. 285–288. [CrossRef]
24. Liu, H.; Chu, R.; Tang, Z. Metal Oxide Gas Sensor Drift Compensation Using a Two-Dimensional Classifier Ensemble. *Sensors* **2015**, *15*, 10180–10193. [CrossRef]
25. Verma, M.; Asmita, S.; Shukla, K.K. A Regularized Ensemble of Classifiers for Sensor Drift Compensation. *IEEE Sens. J.* **2016**, *16*, 1310–1318. [CrossRef]
26. Wang, Q.; Qi, H.; Liu, F. Time Series Prediction of E-nose Sensor Drift Based on Deep Recurrent Neural Network. In Proceedings of the 2019 Chinese Control Conference (CCC), Guangzhou, China, 27–30 July 2019; pp. 479–3484. [CrossRef]
27. Das, P.; Manna, A.; Ghoshal, S. Gas Sensor Drift Compensation by Ensemble of Classifiers Using Extreme Learning Machine. In Proceedings of the 2020 International Conference on Renewable Energy Integration into Smart Grids: A Multidisciplinary Approach to Technology Modelling and Simulation (ICREISG), Bhubaneswar, India, 14–15 February 2020; pp. 197–201. [CrossRef]
28. Dennler, N.; Rastogi, S.; Fonollosa, J.; van Schaik, A.; Schmuker, M. Drift in a popular metal oxide sensor dataset reveals limitations for gas classification benchmarks. *Sens. Actuators B Chem.* **2022**, *361*, 131668. [CrossRef]
29. Perera, A.; Montoliu, I.; Chaudry, A.; Persaud, K.; Marco, S.; Padilla, M. Drift compensation of gas sensor array data by Orthogonal Signal Correction. *Chemom. Intell. Lab. Syst.* **2010**, *100*, 28–35.
30. Comini, E.; Faglia, G.; Sberveglieri, G.; Pan, Z.; Wang, Z.L. Stable and highly sensitive gas sensors based on semiconducting oxide nanobelts. *Appl. Phys. Lett.* **2002**, *81*, 1869–1871. [CrossRef]
31. Kaur, N.; Singh, M.; Comini, E. One-Dimensional Nanostructured Oxide Chemoresistive Sensors. *Langmuir* **2020**, *36*, 6326–6344. [CrossRef] [PubMed]
32. Sberveglieri, G.; Faglia, G.; Groppelli, S.; Nelli, P.; Taroni, A. A novel PVD technique for the preparation of SnO_2 thin films as C2H5OH sensors. *Sens. Actuators B Chem.* **1992**, *7*, 721–726. [CrossRef]
33. Sberveglieri, G. Classical and novel techniques for the preparation of SnO_2 thin-film gas sensors. *Sens. Actuators B Chem.* **1992**, *6*, 239–247. [CrossRef]

34. Müller, G.; Sberveglieri, G. Origin of Sensor Drift in Metal Oxide Gas Sensors: Effects of Adsorption and Surface Band Bending. *Chemosensors*, *in press*.
35. Moseley, P.T.; Tofield, B.C. *Solid State Gas Sensors*; Adam Hilger: Bristol, UK, 1987. [CrossRef]
36. Moseley, P.T.; Norris, J.; Williams, D.E. *Techniques and Mechanisms in Gas Sensing*; Adam Hilger: Bristol, UK, 1991; ISBN 0750300744.
37. Henzler, M.; Göpel, W. Oberflächenphysik des Festkörpers. In *Teubner Studienbücher Physik*; Springer International Publishing: Cham, Switzerland, 1991; ISBN 3-519-03047-0. [CrossRef]
38. Sze, S.M. *Semiconductor Sensors*; John Wiley & Sons: Hoboken, NJ, USA, 1994; ISBN 0-471-54609-7.
39. Sze, S.M. *Semiconductor Devices; Physics and Technology*; John Wiley & Sons: Hoboken, NJ, USA, 2001.
40. Sze, S.M.; Ng, K.K. *Physics of Semiconductor Devices*, 3rd ed.; John Wiley & Sons: Hoboken, NJ, USA, 2007; pp. 79–124. [CrossRef]
41. Ahlers, S.; Müller, G.; Doll, T. A rate equation approach to the gas sensitivity of thin-film SnO_2. *Sens. Actuators* **2005**, *B107*, 587–599. [CrossRef]
42. Ahlers, S.; Müller, G.; Becker, T.; Doll, T. *Factors Influencing the Gas Sensitivity of Metal Oxide Materials. Encyclopedia of Sensors*; Grimes, C.A., Dickey, E.C., Pishko, M.V., Eds.; The Pennsylvania State University: University Park, PA, USA, 2005; ISBN 1-58883-056-X.
43. Comini, E.; Faglia, G.; Sberveglieri, G. *Solid State Gas Sensing*; Springer Science and Business Media: Berlin, Germany, 2009.
44. Madelung, O. *Festkörpertheorie III*; Springer-Verlag: Berlin/Heidelberg, Germany; New York, NY, USA, 2013; ISBN 9783642654138. (In German)
45. Kröger, F.A.; Vink, H.J. *Solid State Physics: Advances in Research and Applications*; Seitz, F., Turnbull, D., Eds.; Academic: New York, NY, USA, 1956; p. 307.
46. Kim, S.S.; Na, H.G.; Kim, H.W.; Kulish, V.; Wu, P. Promotion of acceptor formation in SnO_2 nanowires by e-beam bombardment and impacts to sensor application. *Sci. Rep.* **2015**, *5*, srep10723. [CrossRef]
47. Westbrook, M.H.; Turner, J.D. *Automotive Sensors*; Institute of Physics Publishing: Bristol, UK; Philadelphia, PA, USA, 1994; ISBN 0-7503-0293-3.
48. Hellmich, W.; Braunmühl, C.B.-V.; Müller, G.; Sberveglieri, G.; Berti, M.; Perego, C. The kinetics of formation of gas-sensitive RGTO-SnO_2 films. *Thin Solid Films* **1995**, *263*, 231–237. [CrossRef]
49. Makeeva, E.A.; Rumyantseva, M.; Gas'Kov, A.M. Kinetics of Interaction of Thick Nanocrystalline SnO_2 Films with Oxygen. *Inorg. Mater.* **2004**, *40*, 161–165. [CrossRef]
50. Kamp, B.; Merkle, R.; Lauck, R.; Maier, J. Chemical diffusion of oxygen in tin dioxide: Effects of dopants and oxygen partial pressure. *J. Solid State Chem.* **2005**, *178*, 3027–3039. [CrossRef]
51. Liu, J.; Gao, Y.; Wu, X.; Jin, G.; Zhai, Z.; Liu, H. Inhomogeneous Oxygen Vacancy Distribution in Semiconductor Gas Sensors: Formation, Migration and Determination on Gas Sensing Characteristics. *Sensors* **2017**, *17*, 1852. [CrossRef] [PubMed]
52. Spannhake, J.; Helwig, A.; Müller, G.; Faglia, G.; Sberveglieri, G.; Doll, T.; Wassner, T.; Eickhoff, M. SnO_2:Sb—A new material for high-temperature MEMS heater applications: Performance and limitations. *Sens. Actuators B Chem.* **2007**, *124*, 421–428. [CrossRef]
53. Cavicchi, R.E.; Semancik, S.; Walton, R.M.; Panchapakesan, B.; DeVoe, D.L.; Aquino-Class, M.I.; Allen, J.D.; Suehle, J.S. Microhotplate gas sensor arrays. In *Chemical Microsensors and Applications IIOK*; International Society for Optics and Photonics: Bellingham, WA, USA, 1999; pp. 38–49. [CrossRef]
54. Schütze, A.; Sauerwald, T. Dynamic operation of semiconductor sensors. In *Semiconductor Gas Sensors*; Woodhead Publishing: Sawston, UK, 2019; pp. 385–412. [CrossRef]
55. Street, R.A. Doping and the Fermi Energy in Amorphous Silicon. *Phys. Rev. Lett.* **1982**, *49*, 1187–1190. [CrossRef]
56. Müller, G.; Kalbitzer, S.; Mannsperger, H. A chemical-bond approach to doping, compensation and photo-induced degradation in amorphous silicon. *Appl. Phys. A* **1986**, *39*, 243–250. [CrossRef]
57. Stutzmann, M. Weak bond-dangling bond conversion in amorphous silicon. *Philos. Mag. Part B* **1987**, *56*, 63–70. [CrossRef]
58. Müller, G. On the generation and annealing of dangling bond defects in hydrogenated amorphous silicon. *Appl. Phys. A* **1988**, *45*, 41–51. [CrossRef]
59. Müller, G. Equilibrium dangling bond densities and its related thin-film alloys. *Appl. Phys. A* **1988**, *45*, 103–107. [CrossRef]
60. Krötz, G.; Wind, J.; Stitzl, H.; Müller, G.; Kalbitzer, S.; Mannsperger, H. Experimental tests of the auto compensation model of doping. *Philos. Mag.* **1991**, *63*, 101–121. [CrossRef]
61. Street, R.A. *Hydrogenated Amorphous Silicon*; Cambridge Solid State Science Series; Cambridge University Press: Cambridge, UK, 2005.
62. Hellmich, W.; Müller, G.; Braunmühl, C.-V.; Doll, T.; Eisele, I. Field-effect-induced gas sensitivity changes in metal oxides. *Sens. Actuators B Chem.* **1997**, *43*, 132–139. [CrossRef]